

DETECTING DETERIORATION BEHIND GFRP WRAP STRENGTHENING OF BRIDGE COLUMNS

Oral Büyüköztürk & Tzu-Yang Yu
Massachusetts Institute of Technology
Dept. of Civil and Environmental Eng.
Cambridge, Massachusetts 02139, USA
obuyuk@mit.edu, youngyu@mit.edu

KEYWORDS: NDE, GFRP-wrapped concrete columns, airborne radar, far-field condition, delamination.

ABSTRACT

A radar NDE (nondestructive evaluation) technique using an airborne antenna operating in the far-field condition is developed for detecting damages such as delamination and concrete cracking in GFRP (glass fiber reinforced polymer)-wrapped concrete columns. The far-field airborne radar (FAR) NDE technique is advantageous for distant measurement of bridge columns in practical applications. Far-field radar measurements were made on artificially damaged specimens in the compact RCS (radar cross section)/antenna range facility. Normal incidence and oblique incidence measurement schemes were applied to study the specular effect in reflected signals. Preliminary measurement results indicate the presence of artificial defects behind the GFRP wraps as shown in the frequency-angle imagery. A finite difference-time domain (FD-TD) numerical simulation capability for the electromagnetic (EM) wave propagation and scattering is developed and applied to GFRP-wrapped concrete cylinders. It is shown that this far-field radar NDE technique has potential in identifying structural damages in the surface regions of concrete columns wrapped with GFRP. The importance of data de-noising and filtering along with further image processing is emphasized and planned for further work.

INTRODUCTION

Fiber-reinforced polymer (FRP) composite jacketing systems have emerged as an alternative to traditional construction, strengthening, and repair of reinforced concrete columns and bridge piers (Steckel et al, 1999). A large number of projects, both public and private, have used this technology and escalating deployment is expected, especially in seismically active regions (Fyfe, 2000). The American Concrete Institute (ACI) has compiled a comprehensive guide to address various design issues (ACI 440.2R-02, 2002). Yet, an efficient and effective structural evaluation technology that is capable of assessing the concrete condition inside the FRP jacketing systems and the integrity of bond between FRP and the concrete has been lacking.

Existing evaluation methods such as visual inspection and sample extraction/testing are labor intensive, time consuming, destructive to structures, and most importantly, unable to provide sufficient information about the extent of damage in structural members confined by FRP jackets. Concrete core conditions cannot be fully revealed until physical removal of the jacketing system unless the member has already been subjected to substantive damage. Partial or complete removal of the jacket may, however, pose a danger of structural collapse. A concrete column could appear safe without showing any sign of damage on the jacket and yet containing a substantial cracked or crumbled concrete core. Such scenario could happen when the structure has undergone a modest seismic event damaging the FRP/concrete system while not causing the ultimate failure of the system. That column may not live up to a second seismic event, however, because of the reduced resistance due to the existing invisible damage in the concrete and in concrete/FRP interface region.

In a recent study (Au and Büyüköztürk, 2005), it was reported that concrete cracking, crumbling, and/or delamination could occur under various degrees of confinement pressure provided by the FRP jacket. Fig.

1 shows the local crumbling failure of concrete in a specimen with high level of confinement. High confinement level is often characterized by column strengthening purposes, should there be a change of functionality or an upgrade for seismic counter-measures (Nanni, 1993; Priestley and Sieble, 1996). Fig. 2 shows a global shear crack failure of concrete in a specimen with relatively low levels of confinement. Low confinement level is provided using less amount of FRP fabrics. Applications include repairing of columns that undergo rebar corrosion and concrete spalling (Fyfe, 2000). Both scenarios are equally common in industrial practices (Howie and Karbhari, 1995). Fig. 3 shows the failure of an actual column wrapped with GFRP (glass FRP). Load-deformation behavior of a FRP-wrapped concrete column demonstrates a bilinear response in which a marked reduction in stiffness is experienced after axial stress reaches a certain level which is higher than that corresponding to an unconfined column. The point at which significant axial stiffness reduction begins is referred to as the kinking point (Au and Büyüköztürk, 2005). Beyond kinking, there is a steady increase in strain until the wrapped concrete system fails with explosive fiber fracture accompanied by concrete cracking in the core. Axial stress-volumetric strain behavior of a GFRP-wrapped concrete specimen is shown in Fig. 4. Levels of damages that may have occurred during the loading stage can be quantified by the use of such relationship. The five stages shown in the figure correspond to (1) intact specimen, (2) maximum volumetric contraction, (3) onset of volumetric expansion, (4) increased volumetric expansion, and (5) imminent ultimate failure.

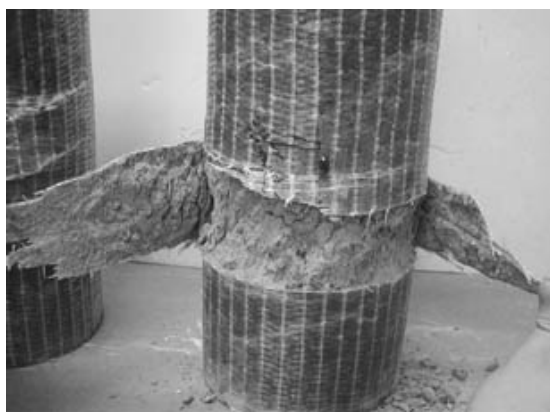


Fig. 1 Local concrete crumbling
(Au and Büyüköztürk, 2005)



Fig. 2 Global shear cracking
(Au and Büyüköztürk, 2005)

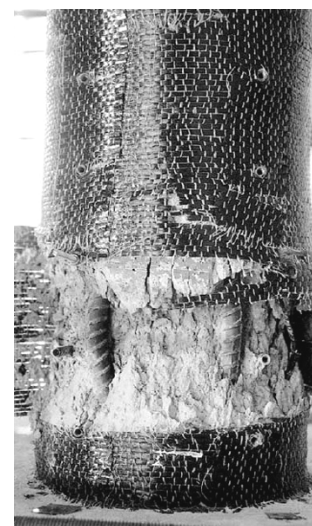


Fig. 3 Column failure
(Sheikh and Yau, 2002)

Existing damages in the interface vicinity, debonding of FRP from concrete, bond delamination between layers of a FRP jacket and those in overlap joints may lead to catastrophic failures at loading stages earlier than those corresponding to intact specimens. Although delamination is often accompanied by discoloring that can be detected by naked eyes (Karbhari et al, 1993), inner ply delamination may not show as well for multi-ply jacketing systems. Overlap joint length reduction due to progressive delamination during a seismic event may also be possible. Overlap joint failures have been reported in laboratory tests regardless of FRP configuration of the jacketing system (Nanni and Bradford, 1995; Au and Büyüköztürk, 2005).

It is clear from the foregoing discussion that a reliable NDE technique needs to be developed for the integrity assessment of FRP-jacketed concrete columns and bridge piers. By visualizing the damage condition via an efficient non-destructive means, decisions can be made regarding time, extent, and cost of a repair scenario after a seismic event or another process causing damage to the structure.

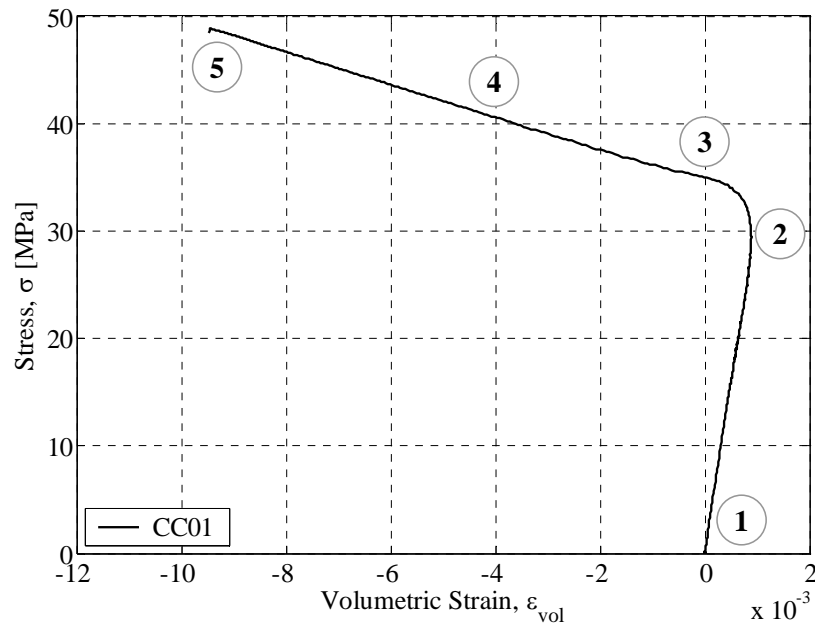


Fig. 4 Axial stress–volumetric strain curves for GFRP-wrapped concrete specimens

In this paper, we summarize our ongoing research dealing with the development of a non-contact NDE technique using far-field airborne radar. This technique aims at the visualization of damages in GFRP-wrapped concrete columns. Damages such as air voids and delaminations in the GFRP-concrete interface region, concrete cracking and crumbling are considered. Far-field radar measurements are made on GFRP-wrapped concrete cylinders with artificially introduced air voids, delaminations and various levels of damages from axial loading. A simulation capability is developed for electromagnetic (EM) wave propagation and scattering phenomenon. Initial results of physical radar measurements and numerical simulations are given.

REVIEW OF NDE TECHNIQUES FOR FRP-WRAPPED CONCRETE

To effectively detect and characterize concrete anomalies and FRP delamination, a NDE technique that is capable of detecting (1) the extent of concrete cracking, crumbling, and FRP delamination from concrete, (2) jacket debonding in the FRP-FRP interface, and (3) sizeable air pockets trapped between FRP and concrete during manufacturing is necessary. Currently, several NDE techniques have been under investigation. They include stress wave (acoustic), infrared thermography, x-ray, and radar (microwave) techniques (Buyukozturk, 1998). Acoustic, infrared thermography, and radar techniques have recently been of particular interest to researchers for possible damage assessment of reinforced concrete and FRP-bonded concrete structures in laboratory settings (Popovics et al, 1994; Tanigawa et al, 1997; Mirmiran et al, 1999; Mirmiran et al, 2001; Bastianini et al, 2001; Feng et al, 2002; Starnes, 2002). In spite of these studies, there is no currently available technology capable of visualizing and characterizing various forms of FRP-bonded concrete damages that is ready for industrial applications.

Acoustic Methods

Acoustic methods are based upon elastic wave propagation in solids. They include pulse-echo, impact-echo, ultrasonic, acoustic emission, and spectral analysis of surface waves (SASW) techniques. Disadvantages include the need of intimate contact between the equipment and subject, the use of sound couplant, as well as the existence of multiple paths through the same subject that make result interpretations difficult (Hillger, 1987).

Infrared Thermography

Infrared thermography is based on the detection of heat flow in the subject in which air gaps resulted from delamination act as insulators, which block out the proper heat flow. Data interpretation is, however, complicated because of varying ambient temperature conditions and surface emissivity variations, which is a function of surface properties (de Vekey, 1990; Starnes, 2002). An attempt was made by Starnes (2002) to quantify subsurface damages of FRP-bonded concrete using infrared thermography.

Radiography

Radiography-based evaluation methods use high frequency electromagnetic radiation (X-rays and Gamma rays) or particular beams (beta rays and neutron radiation) passing through the subject and exposing it onto a film on the other side of the subject. Limitations include the need to access both sides of the subject, the need of safety precautions, long exposure, and two-dimensional (2D) images of three-dimensional (3D) subjects (Malhotra, 1991).

Microwave/Radar Technique

Microwave or radar has been used extensively for site characterization in geotechnical engineering. It has also been used to evaluate concrete structures, pavements, and bridge decks (Fenning and Brown, 1995; Mellet, 1995; Saarenketo and Scullion, 2000). Radar involves the generation and transmission of electromagnetic waves into materials such as concrete with different dielectric constants (Clemena, 1991; Büyüköztürk and Rhim, 1998). Voids, delaminations, rebars, and material characteristics can be detected and interpreted from the reflected waves (Akuthota et al, 2004). Optimization between penetration depths and detection capability, two inversely related parameters that are dependent on the frequencies and bandwidth of the wave, could be a challenge. Conventional radar often makes use of low frequencies to enhance penetration but with sacrificed detectability (Huston et al, 2000). With the proper development of wideband, multi-frequency capability and tomographic imaging techniques, along with measurement of dielectric properties of the subject materials, however, radar can be a powerful tool in assessing structural members that consist of hybrid materials. In this paper, we describe a far-field radar technique for the nondestructive testing of GFRP-wrapped concrete systems.

THE FAR-FIELD AIRBORNE RADAR (FAR) TECHNIQUE

The proposed far-field airborne radar technique mainly consists of an airborne horn antenna, a signal generator, a signal modulator, and an analyzer. In principle, modulated radar signals or EM waves are designed and generated by the signal generator, modulated by the modulator, and transmitted by the horn antenna. The horn antenna is placed beyond the far-field distance from the target structure. Hence the impinging EM waves on the structure will be essentially plane waves. Far-field measurement allows inspections from distance for highway and cross-river bridge columns. Furthermore, the waveform is mathematically simplified for signal processing. The far-field distance will be explained in the later part of this section.

Reflected EM waves or radar signals are collected by the same horn antenna and processed by the analyzer. The radar measurements are collected in inverse (or circular) synthetic aperture radar (ISAR) mode; in other words, the reflected signals are received at different angles with respect to the structure. Image processing algorithms are then applied for processing the reflected signals and for forming the imagery as a basis for condition assessment.

In this section, important radar parameters including pulse width and bandwidth, range and cross-range resolutions, polarization, and radar cross section (RCS) are first introduced. The difference between near-field and far-field is also defined.

Radar Parameters

Pulse Width and Bandwidth

A linear frequency modulated waveform generated by radar consists of a rectangular pulse of duration $T = t_2 - t_1$ as shown in Fig. 5 (a). The carrier frequency f is swept over the pulse length by an amount B which represents the bandwidth, as shown in Fig. 5 (b). For the case of a modulated pulse length similar to T , the swept bandwidth and the achievable pulse are related by (Eaves and Reedy, 1987):

$$T \approx \frac{1}{(f_2 - f_1)} = \frac{1}{B} \quad (1)$$

where f_1 and f_2 are the starting and ending frequencies, respectively.

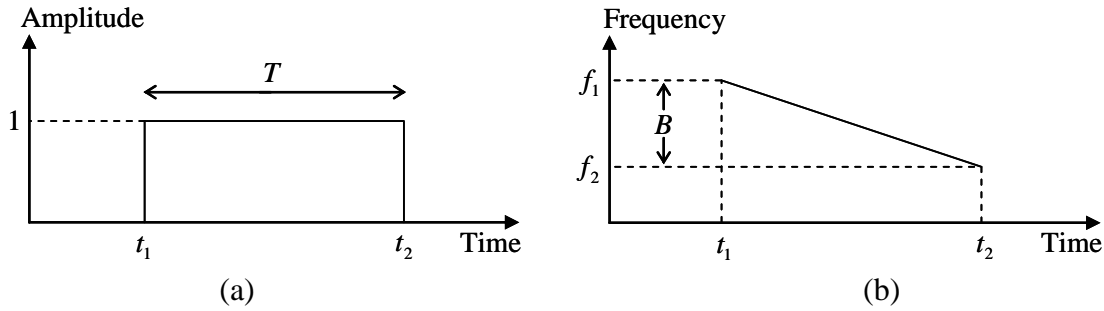


Fig. 5 Linear frequency modulated pulse waveform

Range and Cross-Range Resolutions

Range resolution is defined on the radial (or range) distance from the radar to the target and is obtained from the transmitted signal. Cross-range resolution is related to the resolution perpendicular to the radial direction, and it is obtained by integrating the reflected energy from the target medium as the radar sweeps alongside the area of illumination (Wehner, 1995). The relationships for the range and cross-range resolutions associated with radar are given by the following expressions, respectively (Mensa, 1991; Eaves and Reedy, 1987; Skolnik, 1990; Balanis, 1997):

$$\rho_r \cong \frac{c}{2B} \quad (2)$$

$$\rho_{xr} \cong \frac{\lambda_c}{2\Delta\theta_{rad}} \quad (3)$$

where c = speed of light in free-space, B = bandwidth, λ_c = wavelength at center frequency, and $\Delta\theta_{rad}$ = angular rotation of the target during processing time. Eqs. (2) and (3) are the commonly accepted measure of resolution. Precise expressions are dependent on more specific definitions of resolution (Mensa, 1991). It is worth noticing that the range and cross-range resolution expressions are valid for free-space due to the use of free-space wave velocity. Approximations of these resolutions in a non-magnetic dielectric material (*e.g.* concrete) are given by:

$$\rho_r \approx \frac{\left(\frac{c}{\sqrt{\epsilon_r}}\right)}{2B} \quad (4)$$

$$\rho_{xr} \approx \frac{\left(\frac{c}{f_c \sqrt{\epsilon_r}}\right)}{2\Delta\theta_{rad}} \quad (5)$$

where ϵ_r = dielectric constant of the material and f_c = center frequency.

Polarization

Polarization is defined as the variations of the orientation of electric field with respect to time. Considering that the target under test is an infinite cylinder (treated as a two-dimensional structure), the incident field is referred to as VV-polarized or TM (transverse magnetic) when the electric field is parallel to the axis (infinite dimension) of the cylinder. The other polarization is referred to as HH-polarized or TE (transverse electric) when the electric field is perpendicular to such axis. In the two mentioned polarization options, if the orientation of the electric field does not change with increasing distance, then they are termed linear polarizations. Circular polarization, on the hand, allows for the electric and magnetic field orientations to rotate about the direction of propagation with increasing distance. The availability of the HH and VV polarizations is a key advantage of radar methodologies for NDE applications on anisotropic materials whose properties are dependent on the direction of measurement (Rhim, 1995).

Radar Cross Section (RCS)

Estimation of the signal strength received by a radar receiver requires the knowledge of the signal strength decay of transmitting waves, the response of reflected waves by a remote obstacle, and the dispersion of the reflected waves by the obstacle. A single function σ , referred to as radar cross section (RCS) characterizes the obstacle reflection (Eaves and Reedy, 1987). Formally, RCS is defined as:

$$\sigma = \lim_{r \rightarrow \infty} 4\pi r^2 \frac{|\bar{E}^{scat}|^2}{|\bar{E}^{inc}|^2} \quad (6)$$

where \bar{E}^{scat} and \bar{E}^{inc} are the scattered and incident electric fields (Knott et al, 1987). By its definition, RCS provides information about the target's characteristics and removes the effects of the transmitted power, receiver sensitivity, and the relative distance between the transmitter and receiver.

Near- and Far-field Regions

Antenna patterns vary in shape depending on the distance from the antenna, noted as R , and with the angular direction (polar distribution). In the case of a large distance from the antenna, the shape of the radiation pattern over a sphere of constant radius is independent of R . This distance or the Rayleigh distance is characterized and determined by the far-field condition. Distances satisfying the far-field condition form the far-field region. On the other hand, distances satisfying the near-field condition constitute the near-field region. The discussion of the near-field condition is out of the scope of this paper. In diffraction optics, the near-field is called the Fresnel region, and the far-field is called the Fraunhofer region.

A common accepted far-field condition with $\lambda/16$ wave front error at the far-field distance is

$$R \geq \frac{2D^2}{\lambda} \quad (7)$$

where D = diameter of the smallest sphere that completely contains the antenna, and λ = smallest wavelength of the transmitted wave (Eaves and Reedy, 1987; Wehner, 1995). The far-field distance is found when Eq. (7) is held. Range distances greater than the far-field distance are generally considered in the far-field region.

PHYSICAL RADAR MEASUREMENT

The objective of the exploratory experimental program described in this section is the application of high resolution ISAR radar technologies for the detection and assessment of defect and damage features in GFRP-confined concrete specimens. The experimental set-up, description of test parameters, sample configurations, and data processing are discussed.

Experimental Set-up and Configuration

The radar measurements of GFRP-confined concrete specimens were performed at MIT Lincoln Laboratory using the Compact RCS/Antenna Range facility. The experimental set-up consists of a horn antenna, stepped-frequency radar and network analyzer systems, and a Harris Dual-Shaped reflection system, Model 1606, designed for conducting far-field studies. A photograph of this experimental facility is shown in Fig. 6. The facility can achieve high signal-to-noise ratio measurements for a large frequency bandwidth ranging from UHF (0.7 GHz) to 100 GHz. This radar system is capable of producing a 20-m quiet zone, different antenna radiation patterns, and full polarimetric RCS measurements. Specimens are placed on top of a Styrofoam tower that is capable of fully rotating the target at predetermined angular steps. The measurements were conducted in stepped-frequency mode by sweeping from a starting frequency f_1 to an end frequency f_2 in 0.02 GHz increments at a fixed angle. The target is then rotated to the next angular step and the frequency sweeping is again performed.

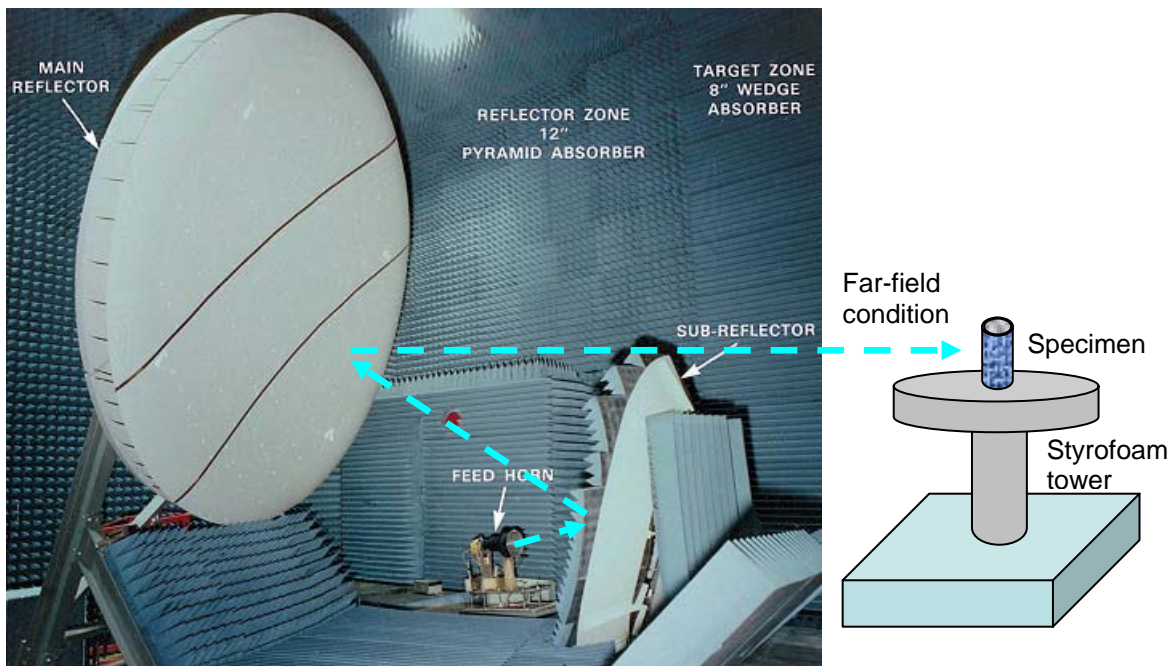


Fig. 6 Compact RCS/antenna range facility [Courtesy of MIT Lincoln Laboratory]

Radar measurements were conducted at X- and Ku-band frequencies (8-12 and 12-18 GHz, respectively) to achieve optimized resolution and surface penetration capabilities. The range resolution is directly related to the bandwidth of radar signals. For X- and Ku-bands whose bandwidths are 4 and 6 GHz respectively, the corresponding range resolutions in free-space are 38 mm and 25 mm. The total rotation angle is 60° in the ISAR measurements and angular increments are 0.1° and 0.2° . Two types of polarizations were used in the radar measurements: HH-polarization and VV-polarization. These measurements were collected in the far-field condition using the facility as shown in Fig. 6.

While the resolution achieved in the radar measurements is significantly high, the trade-off is evident in terms of penetration capabilities. Using the definition of penetration depth for a non-magnetic, dielectric material, the penetration depth is controlled by the permittivity of the material and the measurement frequency. When dielectric losses occur in the material due to conduction currents, the equivalent conductivity σ is expressed as:

$$\sigma = \varepsilon_r'' \varepsilon_0 \omega \quad (8)$$

where ε_r'' is the imaginary part of the complex permittivity, ε_0 is the permittivity of air (in free-space), and ω is the angular frequency.

The determined dielectric constant and loss factor using the proposed dielectric property characterization methodology (Büyüköztürk et al, 2006) for concrete are 5.69 and 0.62, respectively. The estimated penetration depths are approximately 50 mm and 22 mm for 8 and 18 GHz frequencies, respectively. Although the use of high frequency radar waves results in shallow penetration depths, the proposed X- and Ku-bands were originally selected in view of the need to detect near-surface defects, FRP-concrete delaminations, and mechanical damage in the concrete regions close to the FRP jacket.

Specimen Description

Two artificially damaged GFRP-wrapped concrete cylinder specimens were prepared for physical radar measurements (Fig. 7). Artificial damages were introduced by insertion of Styrofoam elements (whose dielectric properties are same as air) on the surface of concrete cylinders, representing construction defect and GFRP delamination. The artificially damaged concrete specimens were then wrapped by GFRP sheet which adhered to concrete with epoxy. The average 28-day strength of the concrete was 26MPa. The water-to-cement ratio was 0.6. The ongoing measurement activity includes GFRP-concrete specimens which are mechanically damaged at different stages as defined in Fig. 4.

In this paper we report preliminary results of measurements on specimens with artificial damages.

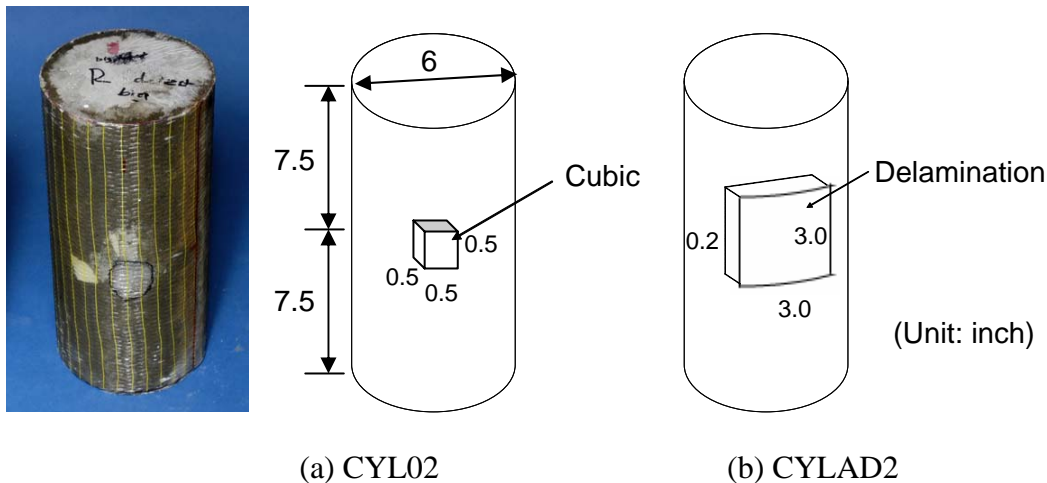


Fig. 7 Two artificially damaged GFRP-concrete specimens

Measurement Schemes

For radar measurements, the specimens under investigation were placed on top of a Styrofoam tower in two alternative orientations: 1) having the specimen rest on one of its ends, referred to as vertical position, and 2) having the specimen rest on its side, referred to as horizontal position. Schematics of the two measurement schemes are presented in Fig. 8. For the specimen with vertical orientation (Fig. 8, left) the angle of incidence θ is at 90° with the z-axis, thus the corresponding radar measurements are always made at normal incidence as the specimen is rotated around its axis. In the oblique incidence scheme (Fig. 8, right), the angle of incidence ϕ varies as the specimen rotates around the y-axis. Normal incidence is encountered only when the direction of incident waves and the axis of the specimen are perpendicular to each other. For all other incidences, the incident wave meets the specimen in an oblique fashion. Both measurement schemes were designed to capture different EM wave scattering behaviors, and consequently investigate their effectiveness when the far-field radar technique is applied for damage or defect detection in GFRP-confined concrete elements.

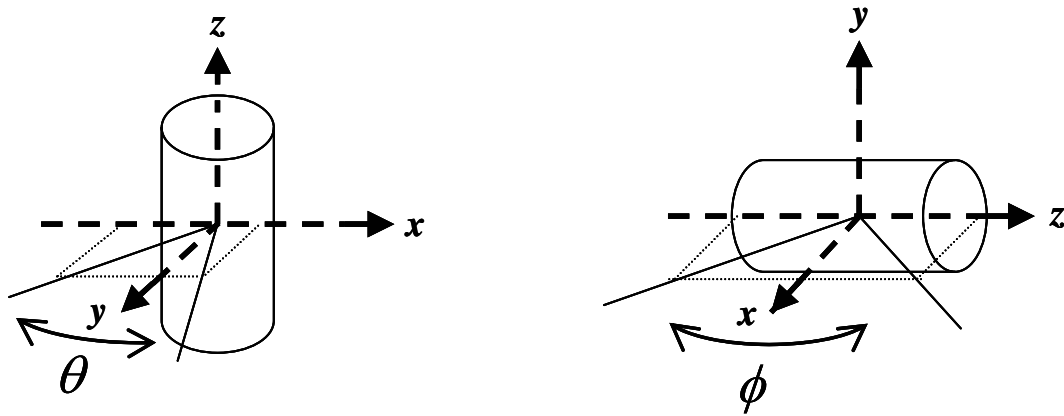


Fig. 8 Normal incidence (left) and oblique incidence (right)

Measurement Results

The radar measurements were collected in ISAR mode, and they consisted of HH and VV polarization measurements as functions of frequency at fixed incident angles. For each polarization, an amplitude entry and a phase entry were recorded at each frequency step. Measurement results are processed and rendered in frequency vs. angle imagery as shown in Figs. 9~12. Only HH polarization (TE wave) measurements are shown. Fig. 9 shows the far-field radar measurements in HH polarization at X-band from intact (without defect) and damaged (with defect) surfaces of the specimen CYL02 using normal incidence scheme. Fig. 10 shows the normal incidence measurements at Ku-band also from the specimen CYL02. Fig. 11 shows the oblique incidence measurements from the specimen CYL02 at X-band. Fig. 12 compares the normal and oblique incidence measurements from the specimen CYLAD2 at X-band.

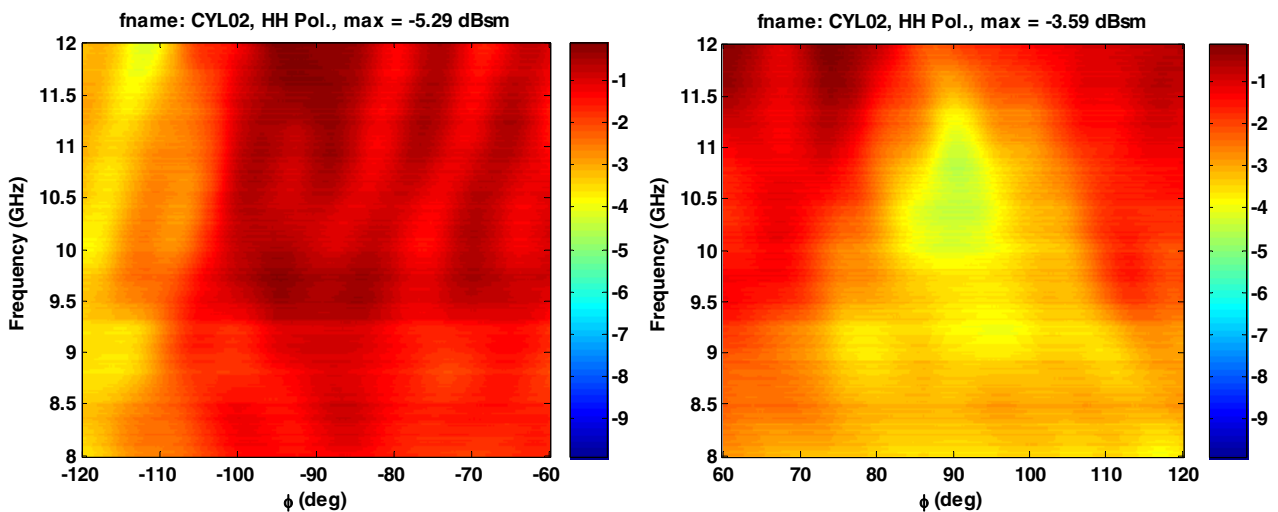


Fig. 9 Frequency – angle imagery for specimen CYL02 measured at normal incidence, X-band, HH polarization, intact (left) and damaged (right) surfaces

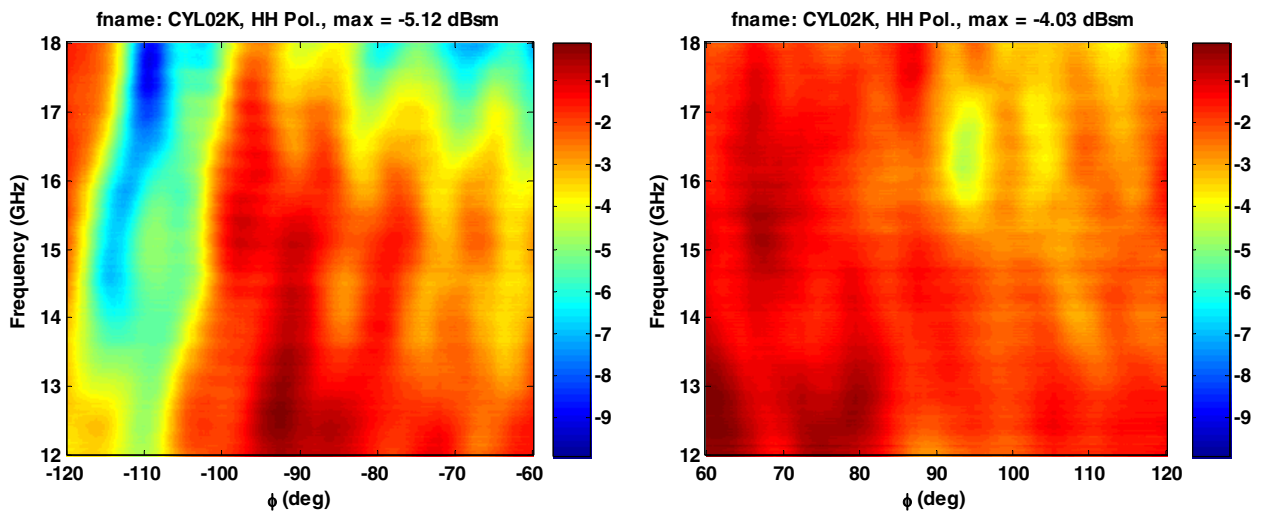


Fig. 10 Frequency – angle imagery for specimen CYL02 measured at normal incidence, Ku-band, HH polarization, intact (left) and damaged (right) surfaces

Discussion

From the normal incidence measurements shown in Fig. 9 it is found that a weak power response area was observed at 90° in the image of damaged surface at X-band, where the artificial defect is embedded underneath the GFRP layer. Since the defect region is consisted of Styrofoam whose dielectric constant is smaller than concrete, the reflection response obtained from the defect region is weaker than the one from intact regions. This weak response area suggests the presence of the defect in that location (90°). Such area is also found in the image of higher frequency ranges (Ku-band, Fig. 10). However, in this case, due to the specular effect, the difference in the power responses between intact and damaged regions is not constantly significant. Surface condition of the specimen, such as roughness, affects the power measurement in higher frequency ranges, especially for reflection signals.

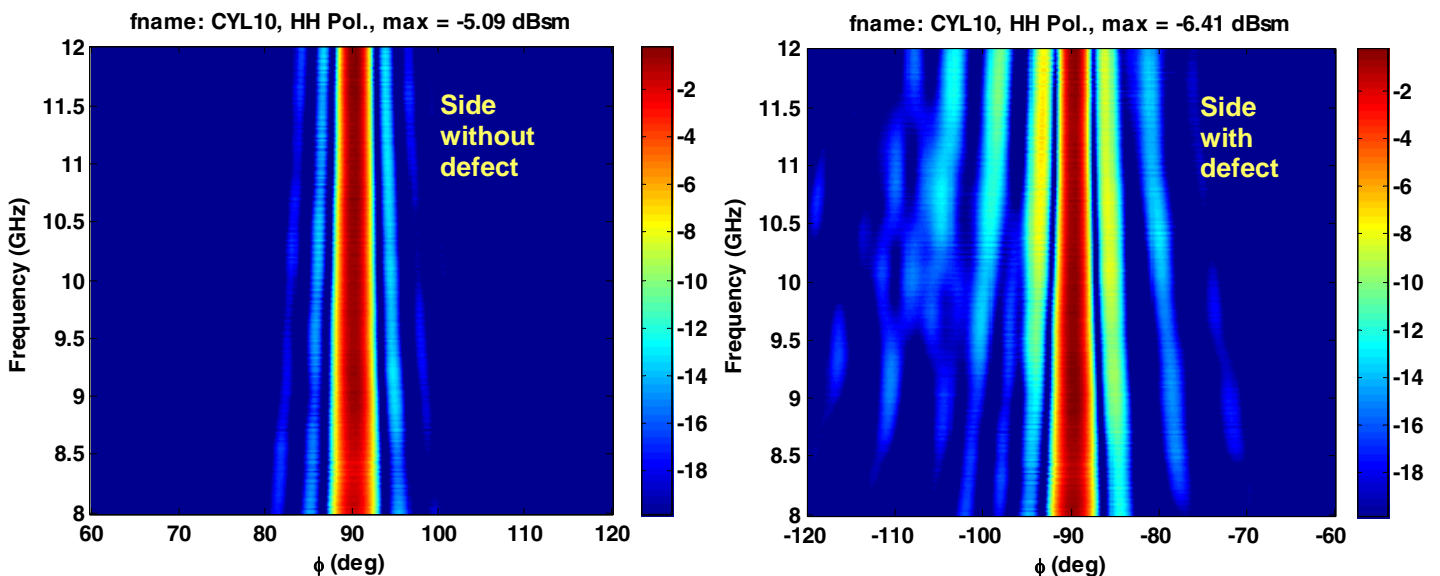


Fig. 11 Frequency – angle imagery for specimen CYL02 measured at oblique incidence, X-band, HH polarization, intact (left) and damaged (right) surfaces

To avoid the specular effect, oblique incidence was adopted and the results are shown in Figs. 11 and 12. The comparison between the responses of intact and damaged surfaces gives a clear indication on the presence of the defect, especially at angles in the vicinity of normal incidence (specular response).

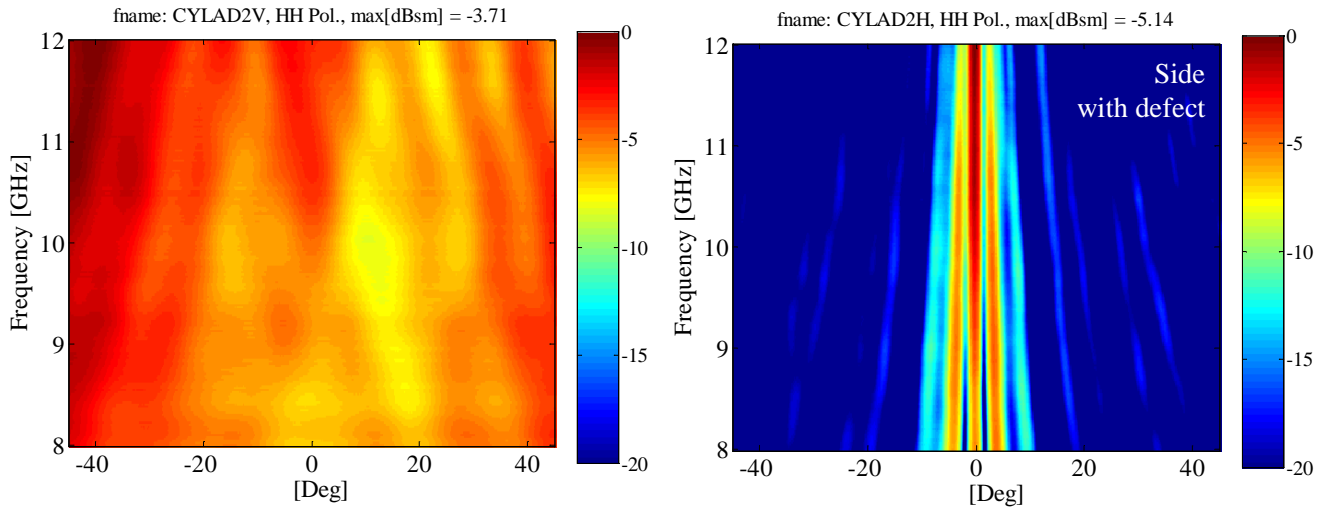


Fig. 12 Frequency – angle imagery for specimen CYL AD2 (delamination) measured at normal and oblique incidences, X-band, HH polarization, both damaged surface

Fig. 12 shows the far-field measurements on specimen CYLAD2 in normal and oblique incidence schemes. Comparing the normal incidence responses of specimens CYL02 and CYLAD2 it is found that the observed weak response area in Fig. 9 cannot be clearly identified in Fig. 12, although an area with rough boundary is observed in the relatively lower frequency ranges in Fig. 12. It is because the thickness of the defect in Fig. 12 is less than the one in Fig. 9, while scattering signals of the defect are also covered by the specular return in both Figs. 9 and 12 which further reduces the detectability of such representation. On the other hand, oblique incidence measurements in Fig. 12 clearly indicate the presence of the defect.

NUMERICAL SIMULATION

A computer program written in Matlab that is capable of simulating EM wave propagation and scattering in the far-field condition was developed. The EM wave propagation and scattering phenomena were simulated in a computational domain using finite-difference time-domain (FD-TD) methods. Central difference scheme was applied and Yee's algorithm was adopted for time and space stepping calculations (Yee, 1966). Temporal and spatial sampling rates satisfied Nyquist's theorem (Hamming, 1989) and Courant-Friedrichs-Lewy (CFL) stability criterion (Taflove and Brodwin, 1975). Perfectly matched layered (PML) (Berenger, 1994) boundary condition was applied to generate nonreflecting boundaries as the absorbing boundary condition (ABC) surrounding the rectangular computational domain. Physical principles and numerical simulation issues are explained as follows.

Source-Free Maxwell's Curl Equations

The relationship between EM fields, namely, electric and magnetic fields, and the medium is governed and explained by Maxwell's equations. Among their several forms in representation, the curl form is most straightforward for differential-based numerical implementation such as finite difference methods. In view of the constraints of limited computational source (degree-of-freedom) and required computational efficiency, only the necessary size of computational domain should be modeled. Furthermore, by using Huygen's principle, an equivalent source can be applied on a closed loop surrounding the structure in far-field radiation problems (Kong, 2000). Therefore, there will be no source in the computational domain for the simulation. The source-free Maxwell' curl equations are

$$\frac{\partial \bar{H}}{\partial t} = -\frac{1}{\mu} \nabla \times \bar{E} - \frac{\sigma^*}{\mu} \bar{H} \quad (9)$$

$$\frac{\partial \bar{E}}{\partial t} = \frac{1}{\varepsilon} \nabla \times \bar{H} - \frac{\sigma}{\varepsilon} \bar{E} \quad (10)$$

where \bar{H} = magnetic field strength (amperes/m), μ = magnetic permeability of the medium (henrys/m), \bar{E} = electric field strength (volts/m), ε = electric permittivity of the medium (farads/m), σ^* = equivalent magnetic loss (ohms/m), and σ = electric conductivity (siemens/m). Eqs. (9) and (10) are the governing equations for calculating the propagation and scattering of EM waves in the computational domain. For the materials considered in this study, $\sigma^* = 0$ (non-magnetic).

Plane Wave Modes

In the far-field region where EM waves are planar in nature, two wave propagation modes are classified by their polarization; VV-polarized or TM waves and HH-polarized or TE waves. The component-level governing equations are expanded from Eqs. (9) and (10) with $\sigma^* = 0$:

$$\text{HH (TE waves): } \frac{\partial E_x}{\partial t} = \frac{1}{\varepsilon} \left[\frac{\partial H_z}{\partial y} - \sigma E_x \right], \quad \frac{\partial E_y}{\partial t} = -\frac{1}{\varepsilon} \left[\frac{\partial H_z}{\partial x} - \sigma E_y \right], \quad (11, 12)$$

$$\left[\frac{\partial^2}{\partial x^2} + \frac{\partial^2}{\partial y^2} - \mu \varepsilon \frac{\partial^2}{\partial t^2} \right] H_z - \sigma \left(\frac{\partial E_y}{\partial x} + \frac{\partial E_x}{\partial y} \right) = 0 \quad (13)$$

$$\text{VV (TM waves): } \frac{\partial H_x}{\partial t} = -\frac{1}{\mu} \left[\frac{\partial E_z}{\partial y} \right], \quad \frac{\partial H_y}{\partial t} = \frac{1}{\mu} \left[\frac{\partial E_z}{\partial x} \right] \quad (14, 15)$$

$$\left[\frac{\partial^2}{\partial x^2} + \frac{\partial^2}{\partial y^2} - \sigma \frac{\partial}{\partial t} - \mu \varepsilon \frac{\partial^2}{\partial t^2} \right] E_z = 0 \quad (16)$$

Finite Difference-Time Domain (FD-TD) Methods

The finite difference (FD) solution to differential equations is obtained by replacing continuous space derivatives with discrete approximations to certain order of accuracy based on Taylor's series expansion. When discretization is also carried out in time, a finite-difference time-domain (FD-TD) solution is obtained. Following the Yee's notation and stepping scheme (Yee, 1966), the central difference solution to Eqs. (11) ~ (16) gives the FD-TD solution of Maxwell's curl equations. Only the FD-TD solution to Eq.(11) is provided here.

$$E_x \Big|_{i,j+1/2,k+1/2}^{n+1/2} = \left(\frac{1 - \frac{\sigma_{i,j+1/2,k+1/2} \cdot \Delta t}{2\varepsilon_{i,j+1/2,k+1/2}}}{1 + \frac{\sigma_{i,j+1/2,k+1/2} \cdot \Delta t}{2\varepsilon_{i,j+1/2,k+1/2}}} \right) E_x \Big|_{i,j+1/2,k+1/2}^{n-1/2} + \left(\frac{\frac{\Delta t}{\varepsilon_{i,j+1/2,k+1/2}}}{1 + \frac{\sigma_{i,j+1/2,k+1/2} \cdot \Delta t}{2\varepsilon_{i,j+1/2,k+1/2}}} \right) \left[\frac{H_z \Big|_{i,j+1,k+1/2}^n - H_z \Big|_{i,j,k+1/2}^n}{\Delta y} - \frac{H_y \Big|_{i,j+1/2,k+1}^n - H_y \Big|_{i,j+1/2,k}^n}{\Delta z} \right] \quad (17)$$

where $E_x \Big|_{i,j+1/2,k+1/2}^{n+1/2}$ denotes the x-component of electric field in space $(i, j+1/2, k+1/2)$ and in time step $t = n+1/2$, other EM field components are also denoted by the same rule; $\sigma_{i,j+1/2,k+1/2}$ and $\varepsilon_{i,j+1/2,k+1/2}$ are

the electric conductivity and permittivity of the medium in space $(i, j+1/2, k+1/2)$, respectively; Δx , Δy , and Δz are the spatial increments and Δt is the temporal increment.

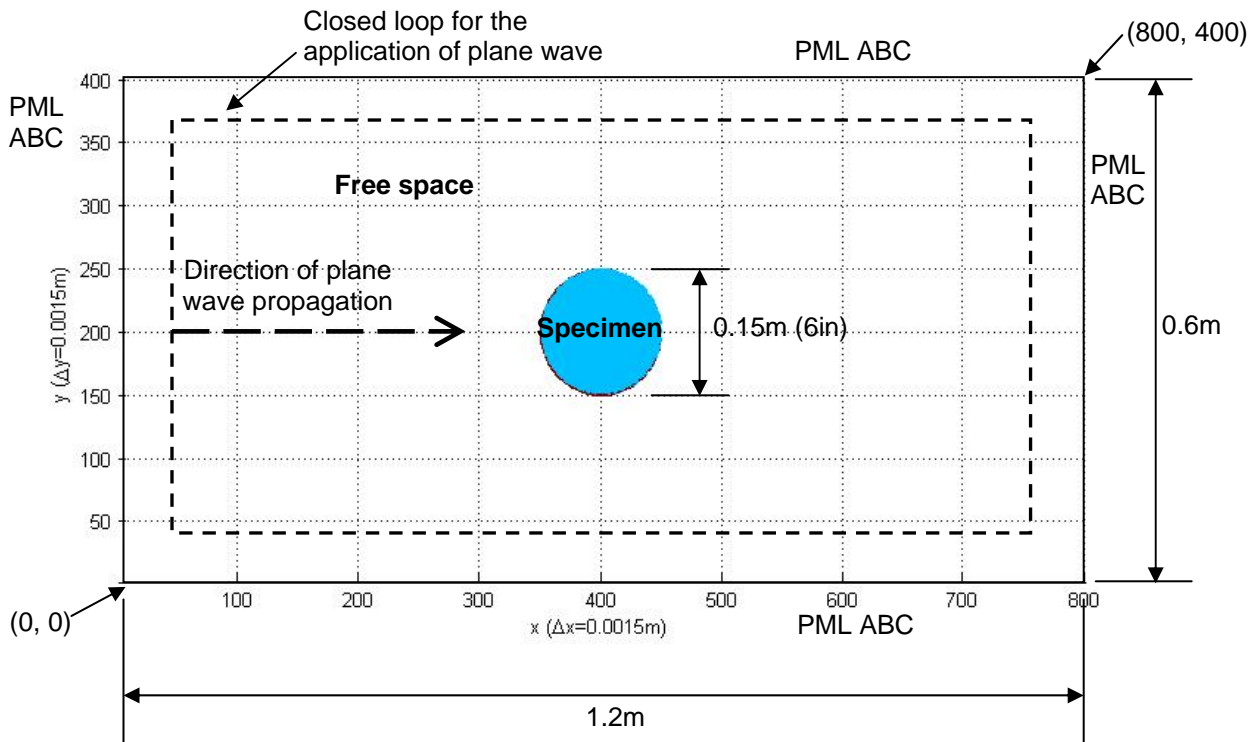


Fig. 13 Modeling of the specimen and the computational domain

Computational Domain and Spatial and Temporal Increments

A rectangular computational domain is prepared in a two-dimensional Cartesian coordinate system for simulating the EM wave propagation and scattering phenomena. The minimum wavelength in X- and Ku-bands is 0.017m (0.7in), suggesting the maximum spatial increment should be smaller than 0.0017m. The implemented spatial increment in the simulation is thus chosen as 0.0015m. Spatial increment is consequently governed by the CFL stability criterion and is selected to be 2.5×10^{-13} sec while satisfying the Nyquist's sampling theorem. A schematic of the computational domain is shown in Fig. 13.

Loading Function

Modulated Gaussian signals are used for the plane TE (HH-polarized) wave loading function with half-power bandwidth = 4GHz. The loading function with central frequency = 8GHz is illustrated in time and frequency domains in Fig. 14. This loading function is used for producing the scattered EM fields. Signals of the same waveform but different central frequencies are applied in the comparison between measurement and simulation.

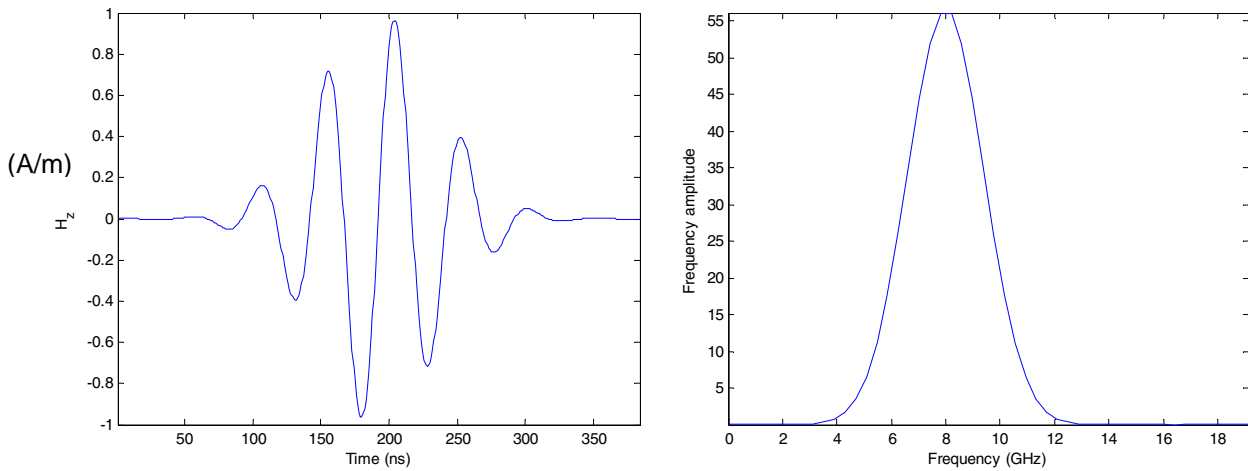


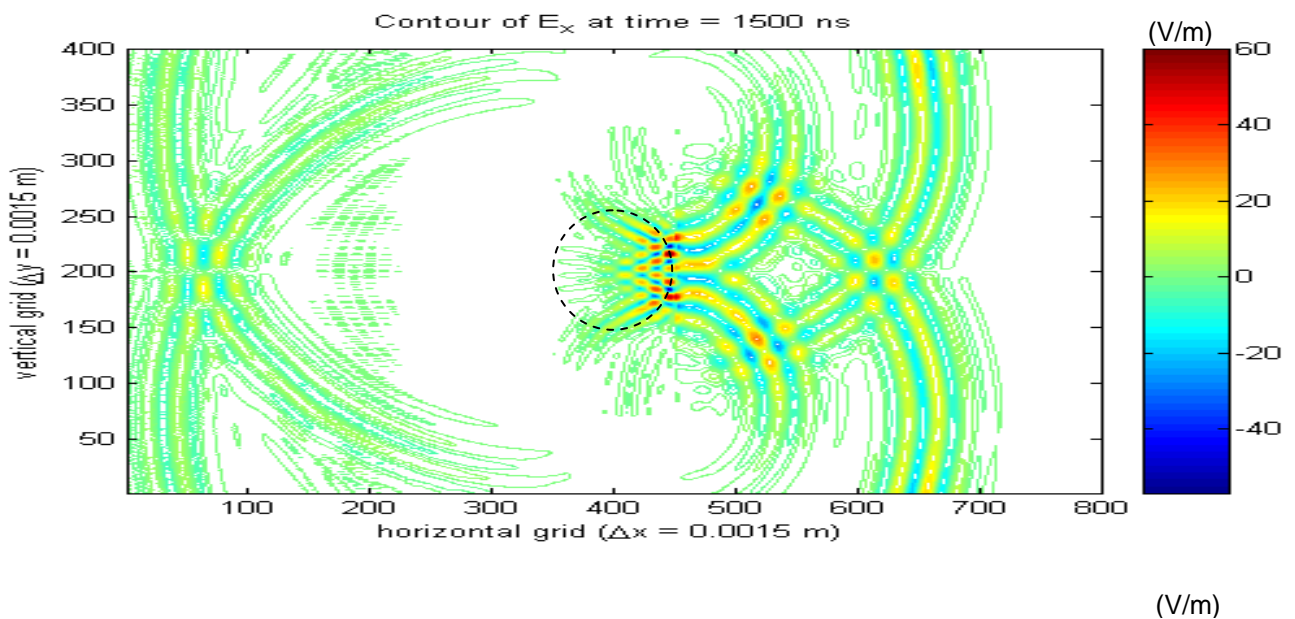
Fig. 14 8GHz loading function in time and frequency domains

Dielectric Properties of Materials

The dielectric properties of materials (concrete, epoxy, and GFRP) are determined by an integrated methodology proposed by the authors. The methodology consists of two main components: (1) an estimation procedure of the real part of complex permittivity based on time difference of arrival (TDOA) information, and (2) a root-searching procedure of possible combinations of real and imaginary parts of complex permittivity based on parametric system identification and SSE (error sum of square) criterion. Detailed description of the methodology can be found in the reference (Büyüköztürk et al, 2006). In the simulation, dielectric constants and loss factors used are 5.69 and 0.62 for concrete, 4 and 0.001 for GFRP-epoxy, respectively.

Scattered EM Fields

Simulated EM wave propagation and scattering are generated from intact and damaged surfaces of the CYL02 specimen with the loading function described above. Snapshots of the EM fields (TE wave: E_x , E_y , and H_z) at time = 1500ns are captured and provided in Figs. 15 (intact response) and 16 (damaged response). Complex EM wave scattering phenomenon due to the presence of the GFRP-concrete cylinder is observed. Differences in EM fields between intact and damaged responses are computed and shown in Fig. 17. These differences in EM fields represent the response solely due to the defect.



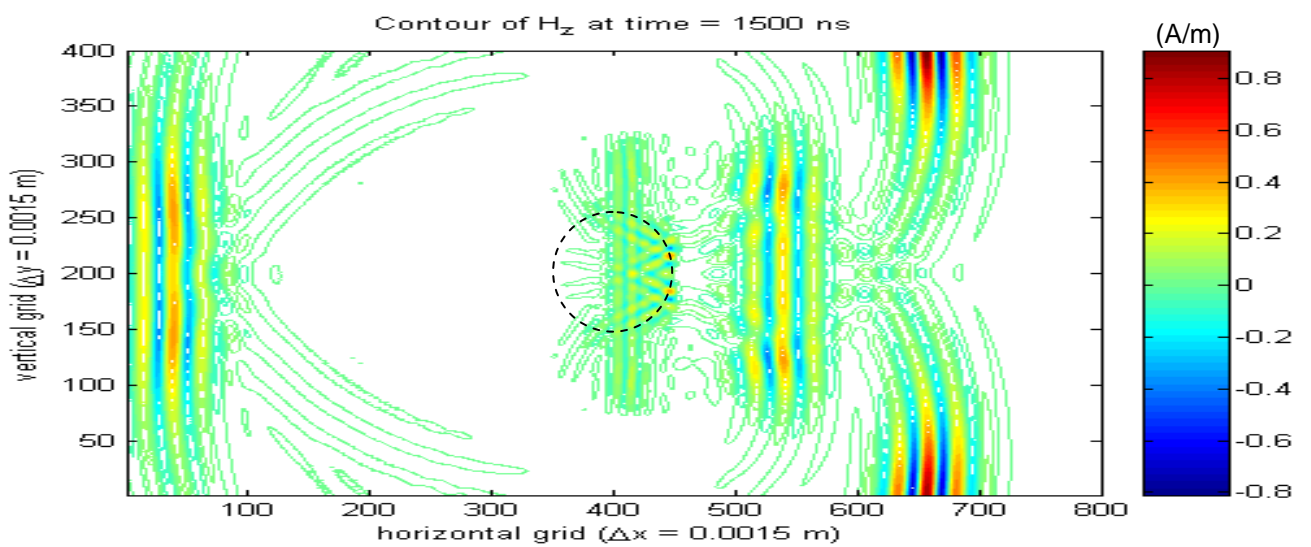
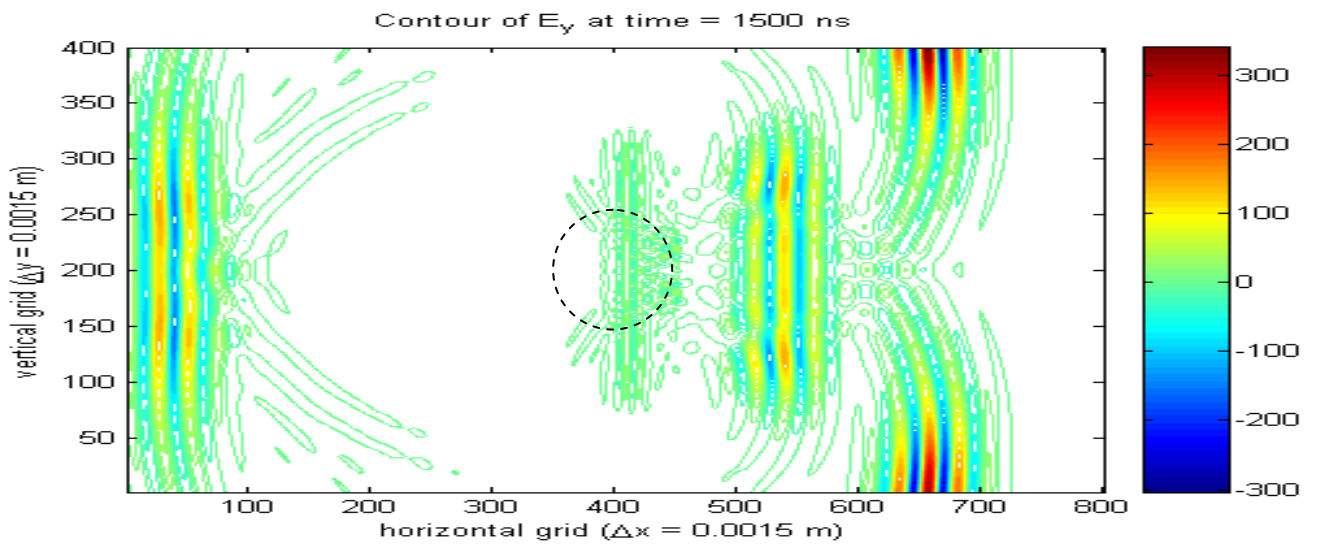
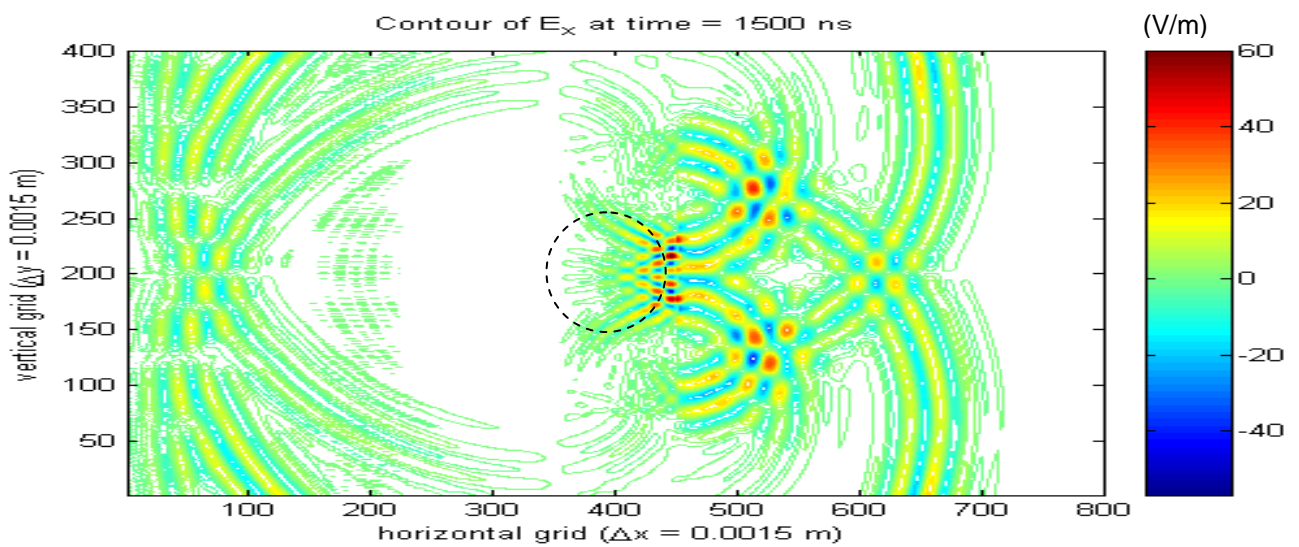


Fig. 15 Scattered EM fields at time = 1500ns from the intact specimen



(V/m)

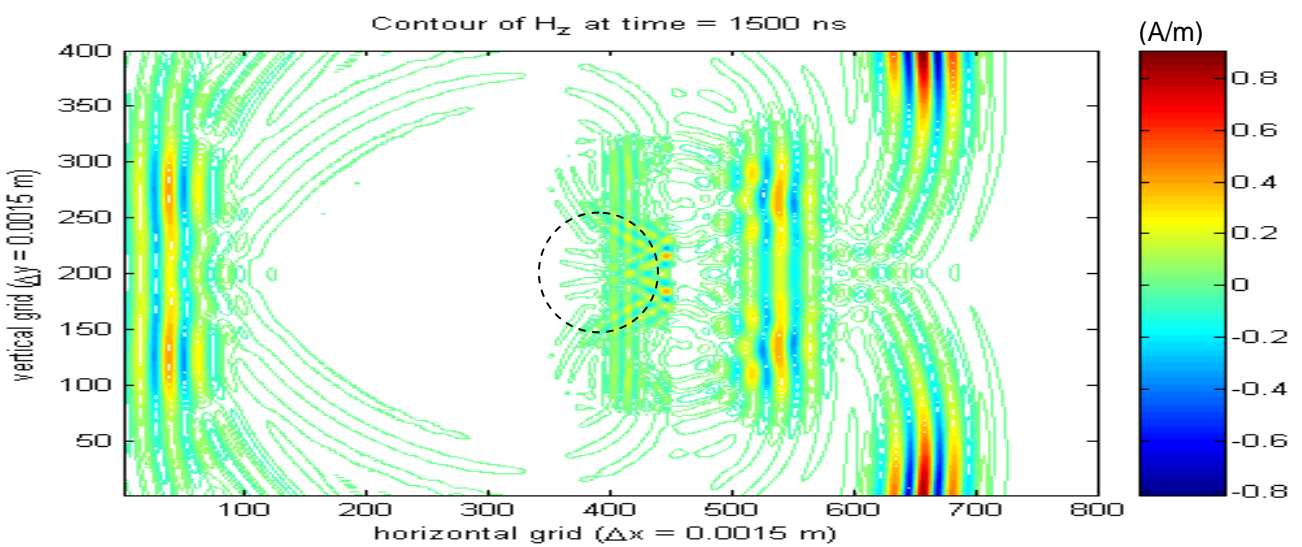
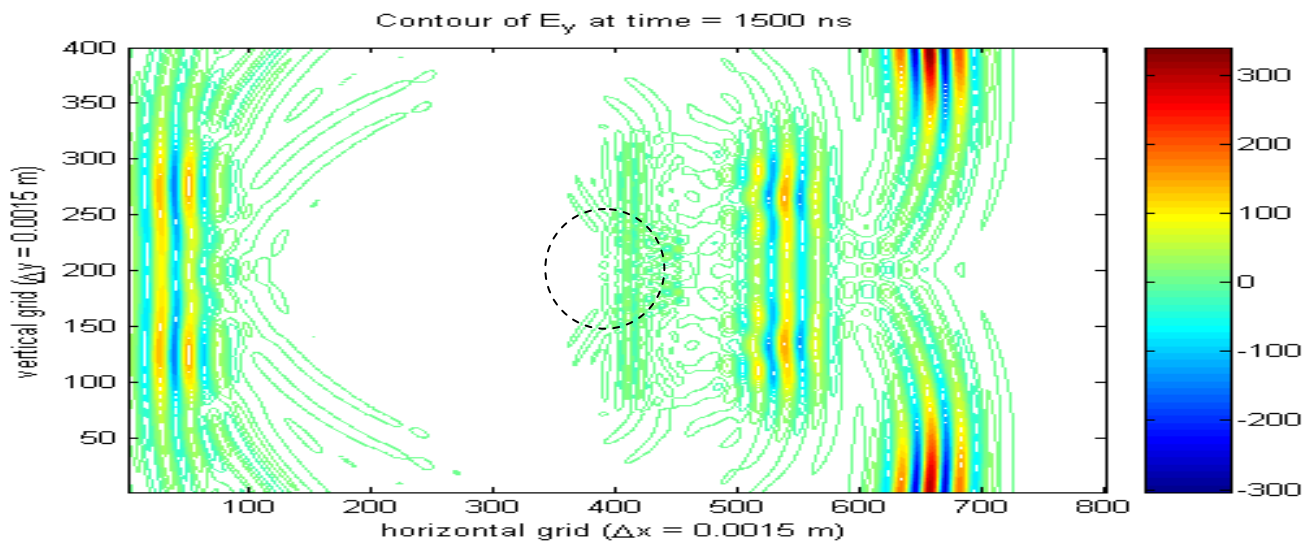
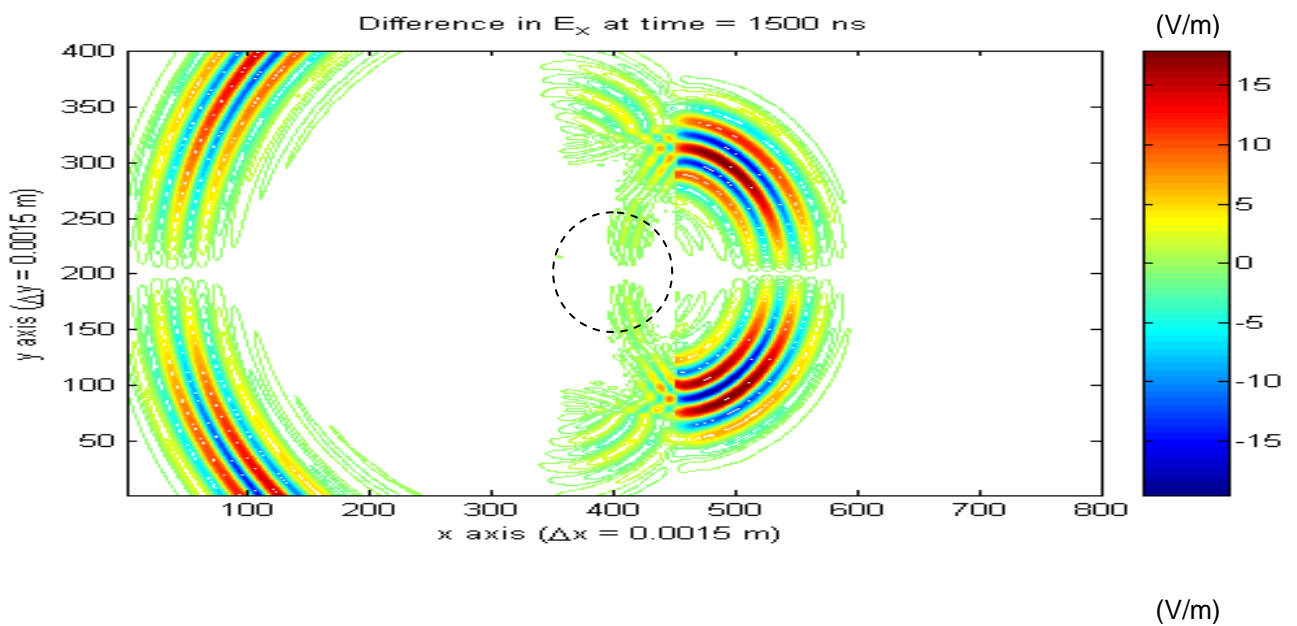


Fig. 16 Scattered EM fields at time = 1500ns from the damaged specimen



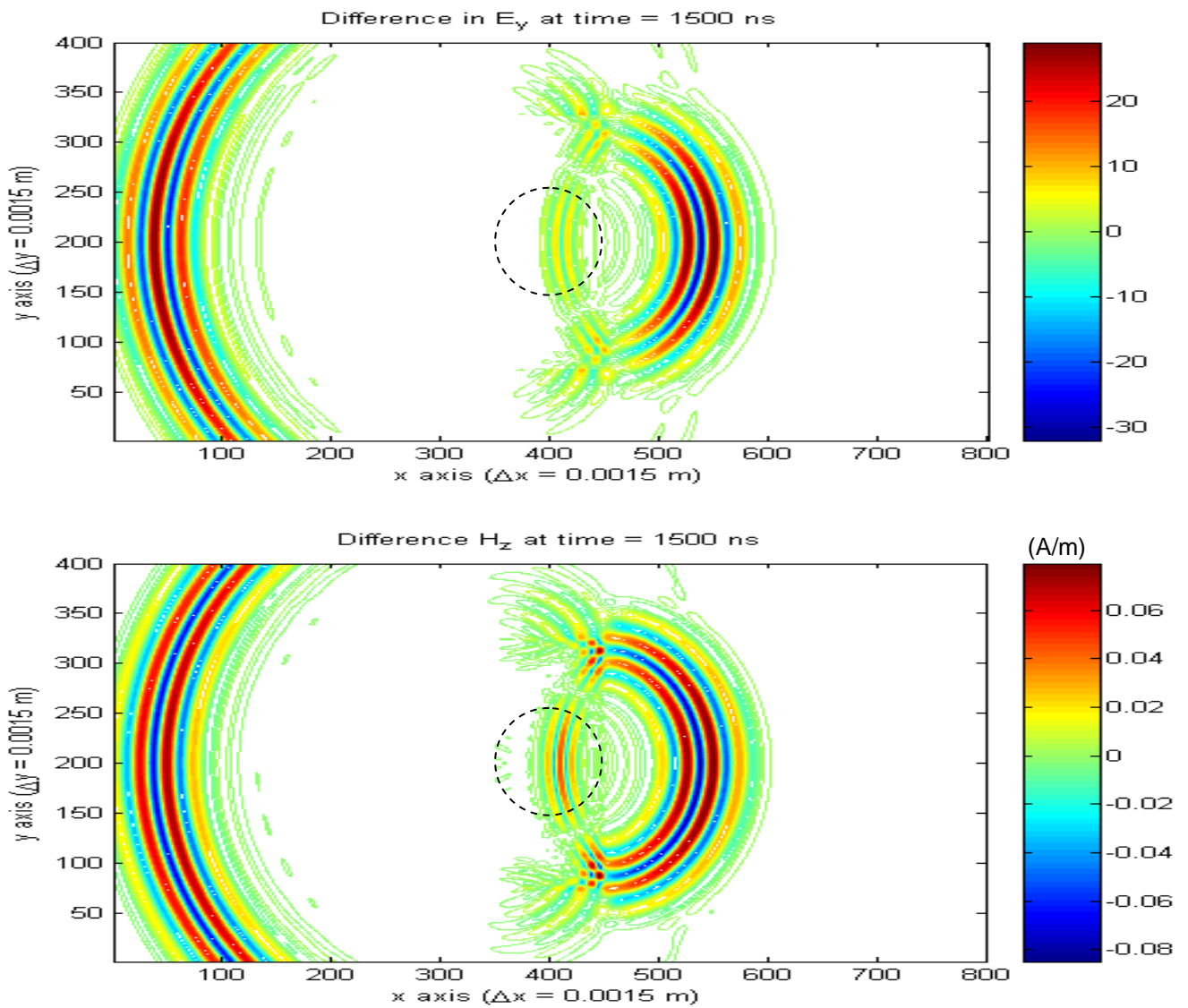


Fig. 17 Differences in the scattered EM fields at time = 1500ns

Comparison between Measurement and Simulation

The comparison of reflected radar signals obtained from physical radar measurement and numerical simulation is shown in Fig. 18. Numerical model is constructed based on the specimen CYL02 representing construction defect as shown in Fig. 7. Fig. 18 shows the far-field power response of the specimen CYL02 represented by frequency-angle imagery. Fig. 19 shows the contour representation of the power response shown in Fig. 18.

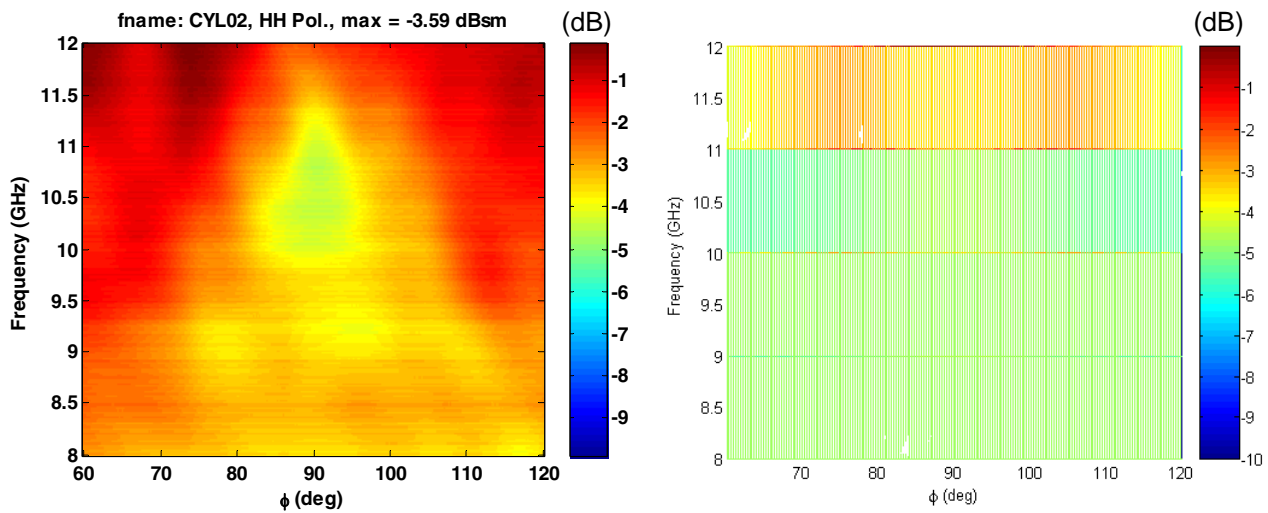


Fig. 18 Frequency – angle imagery of measurement (left) and simulation (right) normal incidence, X-band, HH polarization, front surface (with defect)

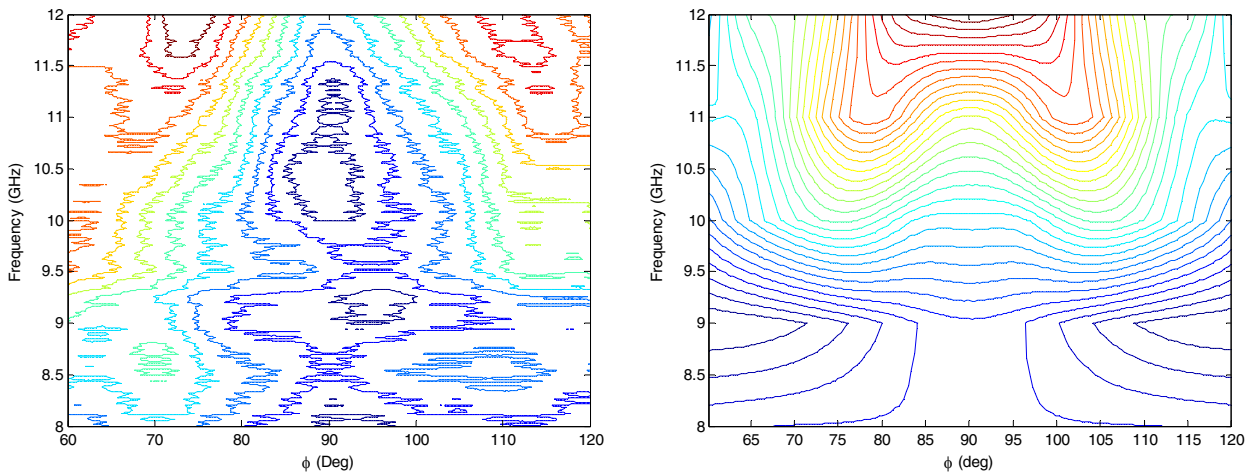


Fig. 19 Contour of the frequency – angle imagery of measurement (left) and simulation (right) normal incidence, X-band, HH polarization, front surface (with defect)

Simulation response is considered to be correlated to the measurement result because they are of same order of power amplitude (Fig. 18) and of similar distribution pattern. The real radar measurement collected in the far-field condition shown in Figs. 18 and 19 indicates the importance of de-noising. Further filtering and processing tasks are needed and are the focus of ongoing research activities in this study.

CONCLUSION

A far-field airborne radar (FAR) NDE technique aiming at the damage detection in the surface region of GFRP-wrapped concrete structures is proposed. To validate the feasibility of the technique physical radar measurements and numerical simulations were performed. Physical radar measurements on GFRP-wrapped concrete cylinder specimens with artificially introduced air voids and delamination behind the GFRP layer were collected at X- and Ku-bands in a compact/radar cross section antenna facility. The radar antenna operated in inverse synthetic aperture radar (ISAR) mode providing reflection measurements at different angles. Two measurement schemes, normal incidence and oblique incidence, were investigated.

It is found that in the normal incidence measurements, due to the specular effect, the difference in the power responses between intact and damaged regions is not constantly significant. On the other hand, the oblique incidence measurements provide a clear indication on the presence of the defect in the frequency-angle imagery. Measurements at oblique incidence provided superior damage indication than those at normal incidence case, regardless of wave polarization and the thickness of the defect. Surface condition of the specimen such as roughness, affects the reflected power measurements in higher frequency ranges (Ku-band), suggesting the importance of data de-noising and filtering.

Based on the findings from this stage of the research, it is believed that the surface damages (GFRP delamination, concrete cracking) on concrete behind the GFRP layer can be detected by the far-field radar measurements. Further work is underway for radar measurements and numerical simulation of mechanically damaged specimens, and data de-noising and filtering for signal processing. Additional work is planned for ISAR imaging and interpretation of damage patterns.

ACKNOWLEDGEMENT

The support for this work was partially provided by the National Science Foundation through Grant CMS-0324607, and by the MIT Lincoln Laboratory through Grant ACC-376 (Advanced Concepts Committee). Wide-bandwidth radar measurements were performed at MIT Lincoln Laboratory under the supervision of Dennis Blejer. We gratefully acknowledge his efforts and contributions to the research reported in this paper. The authors would like to thank J.A. Ortega, a graduate student, for his help with the experimental work.

REFERENCES

- Akuthota, B., Hughes, D., Zoughi, R., Myers, J., and Nanni, A. (2004), "Near-Field Microwave Detection of Disbond in Carbon Fiber Reinforced Polymer Composites Used for Strengthening Cement-Based Structures and Disbond Repair Verification," *Journal of Materials in Civil Engineering*, ASCE, Vol.16, No.6, December, 540-546.
- ACI-440 Committee (2002), "Guide for the Design and Construction of Externally Bonded FRP Systems for Strengthening Concrete Structures," American Concrete Institute, *ACI-440.2R-02*, Farmington Hills, MI.
- Au, C., and Buyukozturk, O. (2005), "Effect of Fiber Orientation and Ply Mix on Fiber Reinforced Polymer-Confined Concrete," *Journal of Composites for Construction*, ASCE, Vol.9, No.5, October, 397-407.
- Bastianini, F., Tommaso, A.D., and Pascale, G. (2001), "Ultrasonic Non-Destructive Assessment of Bonding Defects in Composite Structural Strengthenings," *Composite Structures*, Vol.53, Issue 4, Sep., 463-467.
- Berenger, J.-P. (1994), "A Perfectly Matched Layer for the Absorption of Electromagnetic Waves," *Journal of Computational Physics*, Vol.114, 185-200.
- Büyüköztürk, O. (1998), "Imaging of Concrete Structures," *NDT&E International*, Vol.31, No.4, 233-243.
- Büyüköztürk, O., and Rhim, H. C., (1998), "Electromagnetic Properties of Concrete at Microwave Frequency Range," *ACI Materials Journal*, Vol.95, No.3, 262-271.
- Clemena, G. G., (1991), "Short-Pulse Radar Methods," *CRC Handbook on Nondestructive Testing of Concrete*, V.M. Malhotra and N.J. Carino (ed.), CRC Press, 253-274, Boca Raton, FL.
- de Vekey, R. C. (1990), "Non-Destructive Evaluation of Structural Concrete: A Review of European Practice and Developments," *Proceedings of Nondestructive Evaluation of Civil Structures and Materials*, National Science Foundation and University of Colorado, Boulder, CO.
- Eaves, J. L., and Reedy, E. K. (1987) *Principles of Modern Radar*, Van Nostrand Reinhold Company, New York, NY.
- Feng, M.Q., Flaviis, F.D., and Kim, Y.J. (2002), "Use of Microwaves for Damage Detection of Fiber Reinforced Polymer-Wrapped Concrete Structures," *Journal of Engineering Mechanics*, ASCE, Vol.128, No.2, 172-183.
- Fenning, P.J. and Brown, A.J. (1995), "Ground Penetrating Radar Investigation", *Construction Repair*, Vol.9, No.6, 17-21.
- Fyfe Co. LLC (2000), *Design Manual for the Tyfo[®] Fibrwrap[®] System Rev.2*, San Diego, CA.
- Hamming, R.W. (1989), *Digital Filters*, 3rd Ed., Prentice-Hall, Englewood Cliffs, NJ.
- Hillger, W., (1987), "Inspection of Concrete by Ultrasonic Testing," *Proceedings of the 4th European Conference on Non-Destructive Testing*, London, UK, Vol.2, 1003-1012.
- Howie I., and Karbhari, V. M. (1995), "Effect of Tow Sheet Composite Wrap Architecture on Strengthening of Concrete Due to Confinement: I – Experimental Studies," *Journal of Reinforced Plastics and Composites*, Vol.14, Sep., 1008-1030.
- Huston, D., Hu, J.Q., Maser, K., Weedon, W., and Adam, C. (2000), "GIMA Ground Penetrating Radar System for Monitoring Concrete Bridge Decks", *Journal of Applied Geophysics*, Vol.43, 139-146.
- Karbhari V. M., Eckel D. A., and Tunis G. C. (1993), "Strengthening of Concrete Column Stubs through Resin Infused Composite Wraps," *Journal of Thermoplastic Composite Metatarsals*, Vol.6, 92-106.
- Kong, J.A. (2000), *Electromagnetic Wave Theory*, EMW Publisher, Cambridge, MA.
- Knott, E. F., Shaeffer, J. F., and Tuley, M. T. (1993), *Radar Cross Section*, 2th ed.. Artech House, Norwood, MA.

- Malhotra, V.M. and Carino, N. J. (ed.), (1991), *CRC Handbook on Nondestructive Testing of Concrete*, CRC Press, Boca Raton, FL.
- Mellet, J.S., (1995), "Ground Penetrating Radar Applications in Engineering, Environmental Management, and Geology", *Journal of Applied Geophysics*, Vol.33, 157-166.
- Mensa, D.L. (1991), *High Resolution Radar Cross-Section Imaging*, Artech House, Norwood, MA.
- Mirmiran, A., Shahawy, M., and Echary, H.E. (1999), "Acoustic Emission Monitoring of Hybrid FRP-Concrete Columns," *Journal of Engineering Mechanics*, ASCE, Vol.125, No.8, 899-905.
- Mirmiran, A., and Wei, Y. (2001), "Damage Assessment of FRP-Encased Concrete Using Ultrasonic Pulse Velocity," *Journal of Engineering Mechanics*, ASCE, Vol.127, No.2, 126-135.
- Nanni, A. (1993), *Fiber-Reinforced-Plastic (FRP) Reinforcement for Concrete Structures: Properties and Applications*, Elsevier, Amsterdam, the Netherlands.
- Nanni, A., and Bradford, N.M. (1995), "FRP Jacketed Concrete under Uniaxial Compression," *Construction & Building Materials*, Vol.9, No.2, 115-124.
- Popovics, J.S., and Rose, J.L. (1994), "Survey of Developments in Ultrasonic NDE of Concrete," *IEEE Transactions on Ultrasonics, Ferroelectrics, and Frequency Control*, Vol.41, No.1, 140-143.
- Priestley, M. J. N., and Seible, F. (1996), *Seismic Design and Retrofit of Bridges*, Wiley, New York, NY.
- Saarenketo, T., and Scullion, T. (2000), "Road Evaluation with Ground Penetrating Radar", *Journal of Applied Geophysics*, Vol.43, 119-138.
- Rhim, H. C. (1995), *Nondestructive Evaluation of Concrete using Wideband Microwave Techniques*. PhD Thesis, Department of Civil and Environmental Engineering, MIT, Cambridge, MA.
- Sheikh, S.A., and Yau, G. (2002), "Seismic Behaviour of Concrete Columns Confined with Steel and Fibre Reinforced Polymers", *ACI Structural Journal*, Vol.99, No.1, Jan-Feb, 72-80.
- Starnes, M.A. (2002), "Development of Technical Bases for Using Infrared Thermography for Nondestructive Evaluation of Fiber Reinforced Polymer Composites Bonded to Concrete", Ph.D. Thesis, Department of Civil and Environmental Engineering, MIT, Cambridge, MA.
- Steckel, G., Hawkins, G., and Bauer, J. (1999), "Durability Issues for Composites in Infrastructure," *Proceedings of the 44th International SAMPE Symposium*, Long Beach, CA, 2194-2208.
- Taflove, A., and Brodwin, M.E. (1975), "Numerical Solution of Steady-state Electromagnetic Scattering Problems Using the Time-dependent Maxwell's Equations", *IEEE Transactions on Microwave Theory and Techniques*, Vol. MTT-23, No.8, 623-630.
- Tanigawa, Y., Yamada, K., and Kiriya, S. (1997), "Frequency Characteristics of AE in Concrete," *Proceedings of JCI*, Japan Concrete Institute, Tokyo, Japan, No. 2, 129-132.
- Wehner D. R. (1995), *High Resolution Radar, 2nd ed.*, Artech House, Norwood, MA.
- Yee, K.S. (1966), "Numerical Solution of Initial Boundary Value Problems Involving Maxwell's Equations in Isotropic Media", *IEEE Transactions on Antennas and Propagation*, Vol. AP-14, No.3, 302-307.